

# Observation of a broadband Lamb shift in an engineered quantum system

Matti Silveri<sup>1,2,\*</sup>, Shumpei Masuda<sup>1,3</sup>, Vasilii Sevriuk<sup>1</sup>, Kuan Y. Tan<sup>1</sup>, Eric Hyyppä<sup>1</sup>,  
Matti Partanen<sup>1</sup>, Jan Goetz<sup>1</sup>, Russell E. Lake<sup>1,4</sup>, Leif Grönberg<sup>5</sup>, and Mikko Möttönen<sup>1†</sup>

<sup>1</sup>*QCD Labs, QFT Center of Excellence, Department of Applied Physics,  
Aalto University, P.O. Box 13500, FI-00076 Aalto, Finland*

<sup>2</sup>*Research Unit of Nano and Molecular Systems,  
University of Oulu, P.O. Box 3000, FI-90014 Oulu, Finland*

<sup>3</sup>*Collage of Liberal Arts and Sciences, Tokyo Medical and Dental University, Ichikawa, 272-0827, Japan*

<sup>4</sup>*National Institute of Standards and Technology, Boulder, Colorado 80305, USA*

<sup>5</sup>*VTT Technical Research Centre of Finland, QFT Center of Excellence, P.O. Box 1000, FI-02044 VTT, Finland*  
(Dated: December 16, 2022)

The shift of energy levels owing to broadband electromagnetic vacuum fluctuations—the Lamb shift—has been pivotal in the development of quantum electrodynamics and in understanding atomic spectra<sup>1–6</sup>. Currently, small energy shifts in engineered quantum systems are of paramount importance owing to the extreme precision requirements in applications such as quantum computing<sup>7,8</sup>. However, without a tunable environment it is challenging to resolve the Lamb shift in its original broadband case. Consequently, the observations in other than atomic systems<sup>1–5,9</sup> are limited to environments comprised of narrow-band modes<sup>10–12</sup>. Here, we observe a broadband Lamb shift in high-quality superconducting resonators, including the static shift inaccessible in Lamb’s experiment<sup>1,2</sup>. We measure a continuous change of several megahertz in the fundamental resonator frequency by externally tuning the coupling strength of the engineered broadband environment which is based on hybrid normal-metal–superconductor tunnel junctions<sup>13–15</sup>. Our results may lead to improved control of dissipation in high-quality engineered quantum systems and open new possibilities for studying synthetic open quantum matter<sup>16–18</sup> using this hybrid experimental platform.

Physical quantum systems are always open. Thus, exchange of energy and information with an environment eventually leads to relaxation and degradation of quantum coherence. Interestingly, the environment can be in a vacuum state and yet cause significant perturbation to the original quantum system. The quantum vacuum can be modelled as broadband fluctuations which may absorb energy from the coupled quantum systems. These fluctuations also lead to an energy level renormalization—the Lamb shift—of the system, such as that observed in atomic systems<sup>1–5,9</sup>. Despite of its fundamental nature, the Lamb shift arising from broadband fluctuations is often overlooked outside the field of atomic physics as a small constant shift that is challenging to distinguish<sup>20</sup>. Due to the emergence of modern engineered quantum systems, in which the desired precision of the energy levels is comparable to the Lamb shift, it has, however,

become important to predict accurately the perturbation as a function of external control parameters. Neglecting energy shifts can potentially take the engineered quantum systems outside the region of efficient operation<sup>21,22</sup> and may even lead to undesired level crossings between subsystems. These issues are pronounced in applications requiring strong dissipation. Examples include reservoir engineering for autonomous quantum error correction<sup>23,24</sup>, or rapid on-demand entropy evacuation<sup>14,15,25</sup>. Furthermore, the role of dissipation in phase transitions of open many-body quantum systems has attracted great interest through the recent progress in studying synthetic quantum matter<sup>16,17</sup>.

In our experimental setup, the broadband environment responsible for the Lamb shift is formed by photon-assisted electron tunneling through normal-metal–insulator–superconductor junctions<sup>14,15,19,26</sup> (Fig. 1). The system exhibiting the Lamb shift is a superconducting coplanar waveguide resonator with the resonance frequency  $\omega_r/2\pi = 4.7$  GHz and 8.3 GHz, respectively for Sample A and B, with loaded quality factors in the range of  $10^2$  to  $10^3$ . The coupling strength between the environment and the resonator  $\gamma_T/2\pi$  can be tuned from 10 kHz to 10 MHz (Fig. 2). The exceptionally broad tuning range makes it possible to accurately observe the Lamb shift, ranging from 0 MHz to 17 MHz. The tuning is controlled with a bias voltage, which shifts the relative chemical potential between the normal-metal and superconductor leads and activates the photon-assisted tunneling when the chemical potential is near the edge of the gap of the superconductor density of states (Fig. 1). Finally, we verify our model by measuring the response of the coupling strength to changes in the normal-metal electron temperature (Fig. 3).

Figure 1a–b describes the measurement scheme (Methods) and the samples, the fabrication of which is detailed in ref. 15. The resonator is capacitively coupled to a normal-metal island which is tunnel-coupled to two superconducting leads. An electron tunneling event between the island and the leads shifts the charge of the resonator by an amount of  $\Delta q = \alpha e$ , where  $\alpha \approx 1$  is a capacitance fraction defined in Fig. 1 and  $e$  is the elementary charge. A tunneling event couples different states of the resonator mode, and can lead to the creation and annihilation of

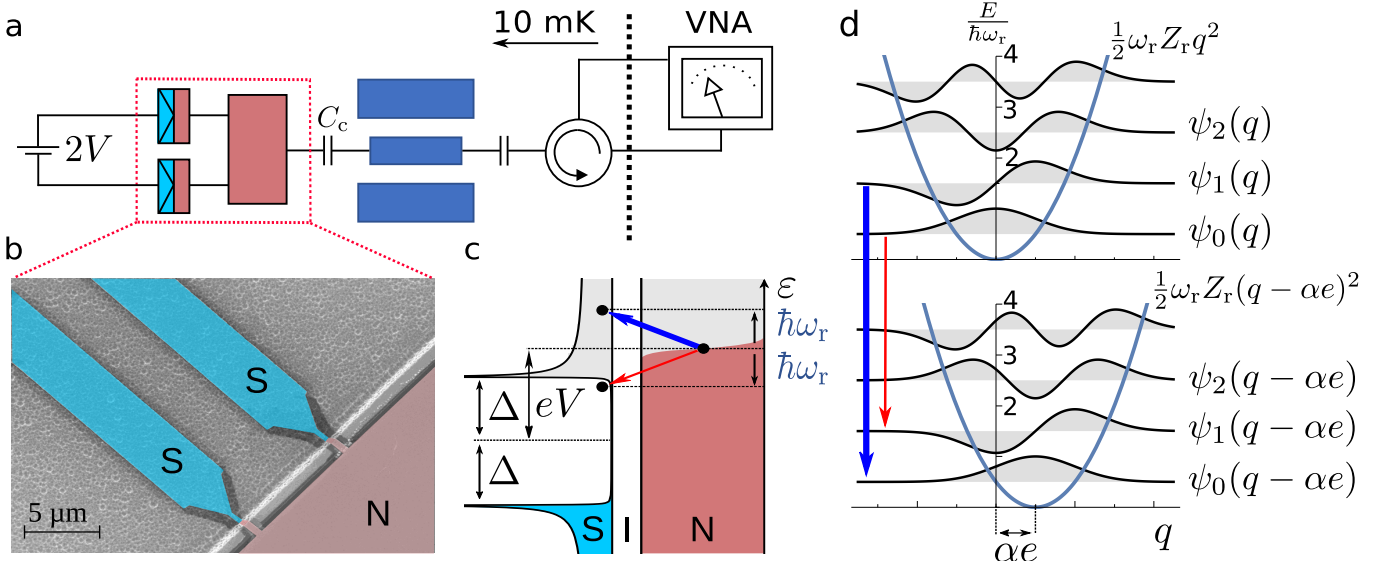


**Figure 1. Sample and measurement setup.** **a**, Schematic illustration of the coplanar waveguide resonator (dark blue) capacitively coupled to a normal-metal island (red) and a transmission line together with a simplified measurement setup. **b**, False-colour scanning electron microscope image of the two superconductor–insulator–normal-metal (SIN) tunnel junctions used as an engineered environment for the resonator modes. See Supplementary Figs. 1–2 for an extended image of the sample and the measurement setup. **c**, Energy diagram of photon-assisted tunneling at a superconductor–insulator–normal-metal junction. In the normal-metal, the electron occupation (red shading) follows the Fermi distribution. The superconductor density of states exhibits the characteristic Bardeen–Cooper–Schrieffer energy gap of magnitude  $2\Delta$ . The states below the gap are filled (blue shading). The gray shading denotes empty states. The blue arrow depicts a tunneling process that absorbs a photon with energy  $\hbar\omega_r$  from the resonator mode at the angular frequency  $\omega_r$ . The red arrow corresponds to photon emission. Elastic processes do not affect the resonator but contribute in the thermalization of the normal-metal island<sup>19</sup>. The bias voltage  $V$  shifts the electrochemical potentials of the normal-metal and the superconductor relative to each other by  $eV$ . For voltage biases  $|eV| < \Delta + \hbar\omega_r$ , emission processes are suppressed by the vanishing density of states in the superconductor gap. **d**, A tunneling event on the normal-metal island shifts the charge of the resonator by  $\Delta q = \alpha e$ . The capacitance fraction  $\alpha = C_c / (C_c + C_{\Sigma m}) \approx 1$  is given by the coupling capacitance  $C_c$  between the resonator and the normal-metal island and the capacitance of the normal-metal island to ground  $C_{\Sigma m}$  (Table I). The charge shift induces transitions between the resonator energy eigenstates  $\psi_i(q)$  and  $\psi_f(q)$  via the matrix element  $|M_{if}|^2 = |\int \psi_f^*(q - \alpha e) \psi_i(q) dq|^2 \propto \rho^{|i-f|}$ , where  $\rho = \pi\alpha^2 Z_r / R_K$  is an interaction parameter expressed in terms of the characteristic impedance  $Z_r$  of the resonator and the von Klitzing constant  $R_K = h/e^2$  containing the Planck constant  $h$  (Methods). The blue and red arrows correspond to the same processes as in **c**.

photons. The rates of these processes are proportional to factors arising from the charge shift, junction transparency, and energy conservation<sup>19</sup> as detailed in Fig. 1c–d (Methods). Note however that a linear resonator is not dephased by charge fluctuations.

The resonator is probed through a  $50\text{-}\Omega$  transmission line in a standard microwave reflection experiment (Fig. 1a). The voltage reflection coefficient  $\Gamma = |\Gamma|e^{-i\varphi}$  of a weak probe signal at the angular frequency  $\omega_p$  is given by

$$\Gamma = \frac{\gamma_{\text{tr}} - \gamma_{\text{T}} - \gamma_0 + 2i(\omega_p - \omega_r)}{\gamma_{\text{tr}} + \gamma_{\text{T}} + \gamma_0 - 2i(\omega_p - \omega_r)}, \quad (1)$$

where  $\gamma_{\text{tr}}$  is the coupling strength to the transmission line and  $\gamma_0$  represents the damping rate of the resonator by excess sources (Methods). Figures 2a–b show the magnitude of the measured reflection coefficient for Sample A and B (for the phase data see Supplementary Fig. 3). At a given bias voltage, the minimum reflection occurring at

$\omega_p = \omega_r$  yields the resonator frequency. The full width of the dip at half minimum equals the total coupling strength  $\gamma_{\text{T}} + \gamma_{\text{tr}} + \gamma_0$ , related to the loaded quality factor by  $Q_{\text{L}} = \omega_r / (\gamma_{\text{tr}} + \gamma_{\text{T}} + \gamma_0)$ . At the critical points, where  $\omega_p = \omega_r$  and  $\gamma_{\text{T}} + \gamma_0 = \gamma_{\text{tr}}$  (the dark spots in Fig. 2a), the reflection ideally vanishes because of the impedance matching between the transmission line and the other electromagnetic environments of the resonator. Thus the full width of the dip  $2\gamma_{\text{tr}}$  gives accurately the coupling strength to the transmission line. The phase of the reflection coefficient exhibits a full  $2\pi$  winding about the critical points (Supplementary Fig. 3). We extract the coupling strengths and the resonator frequency by fitting equation (1) to the data.

Figures 2c–d show the measured voltage-tunable coupling strength  $\gamma_{\text{T}}$  for the two samples. The characteristics of the coupling strength can be understood by considering tunneling at different bias voltages. If the junction is not biased and  $\hbar\omega_r \ll \Delta$ , where the gap parameter  $\Delta$  is

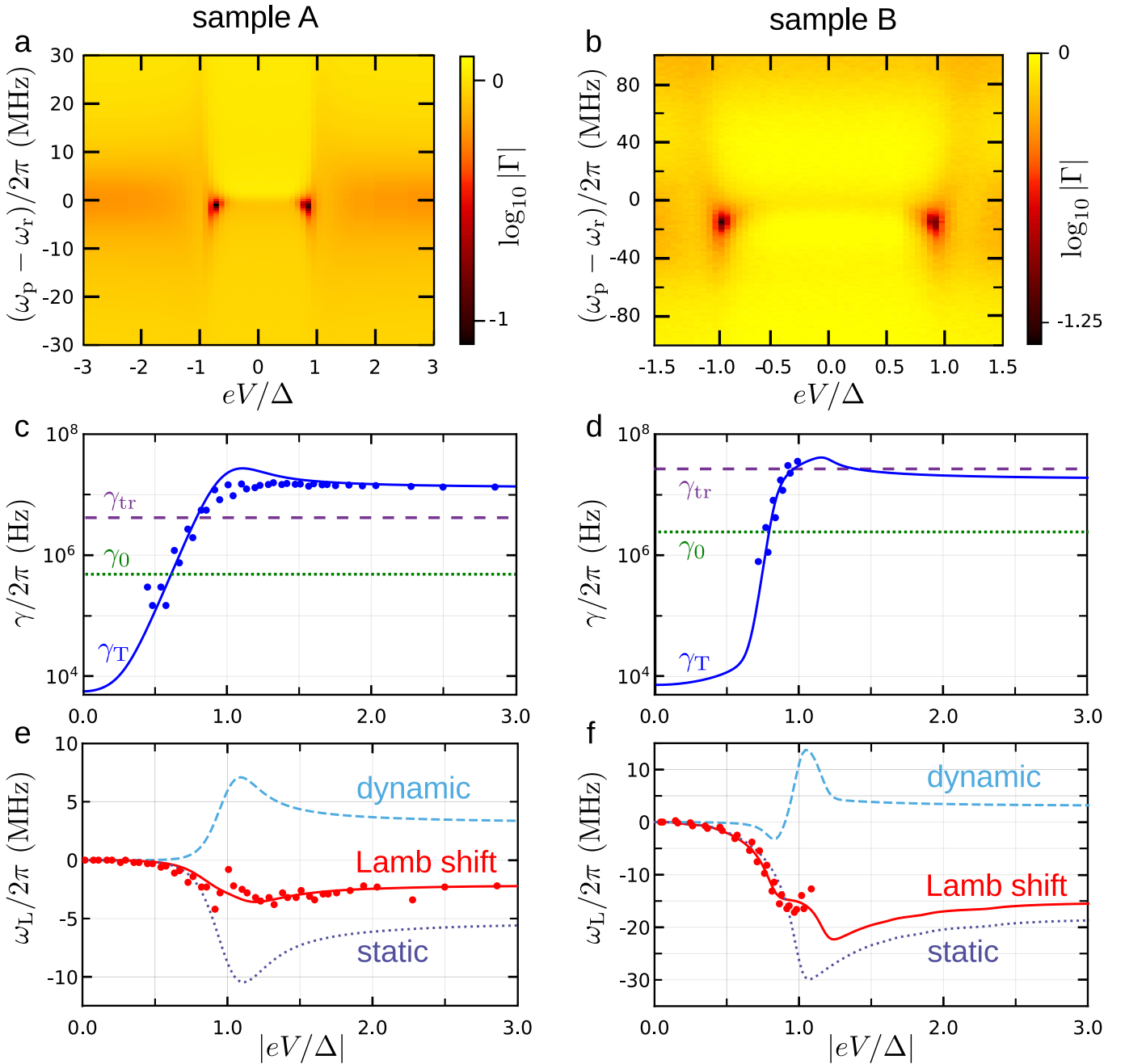


Figure 2. **Observation of the Lamb shift.** **a, b**, Magnitude of the voltage reflection coefficient  $|\Gamma|$  as a function of the probe frequency  $\omega_p$  and the single-junction bias voltage  $V$ . **c, d**, Coupling strength  $\gamma_T$  to the electromagnetic environment formed by the photon-assisted tunneling at the superconductor–insulator–normal-metal junctions as a function of the the single-junction bias voltage  $V$ . For the calculated coupling strengths (solid lines) we use experimentally realized parameter values, see Table I. The horizontal dashed lines denote the coupling strength to the transmission line  $\gamma_{tr}$  and the horizontal dotted lines indicate the coupling strength to excess sources  $\gamma_0$ . **e, f**, The Lamb shift as a function of the single-junction bias voltage  $V$  (solid circles). The solid line denotes the calculated total Lamb shift including both the static (dotted line) and the dynamical (dashed line) parts. Panels **a, c**, and **e** are for Sample A and **b, d**, and **f** correspond to Sample B.

defined in Fig. 1, the tunneling and the resulting coupling strength  $\gamma_T$  are suppressed by the small density of states in the superconductor gap<sup>27</sup>, quantified by the Dynes factor  $\gamma_D \ll 1$ . If the bias voltage is near the gap edge, the electron tunneling is efficiently assisted by thermal energy.

As a result of thermal activation, the coupling strength  $\gamma_T$  increases exponentially as a function of the bias voltage, and reaches its maximum near the gap edge. At high bias voltages  $|eV/\Delta| \gg 1$ , the coupling strength  $\gamma_T$  saturates to the value  $2\alpha^2(Z_r/R_T)\omega_r$ , where  $Z_r$  is the characteristic

Table I. Key device and model parameters

Parameter	Symbol	Sample A	Sample B
Resonator frequency (GHz)	$\omega_r/2\pi$	4.67	8.54
Charac. impedance ( $\Omega$ )	$Z_r$	34.8	34.8
External coupling (MHz)	$\gamma_{tr}/2\pi$	4.2	26.6
Excess coupling (MHz)	$\gamma_0/2\pi$	0.49	2.42
Coupling capacitance (fF)	$C_c$	840	780
Island capacitance (fF)	$C_{\Sigma m}$	10	10
Superconductor gap ( $\mu\text{eV}$ )	$\Delta$	215	195
Dynes parameter	$\gamma_D$	$4 \times 10^{-4}$	$4 \times 10^{-4}$
Junction resistance (k $\Omega$ )	$R_T$	24.5	32.3
Electron temperature (mK)	$T_N$	190	60
Cut-off frequency ratio	$\omega_c/\omega_r$	0.85	2.51

impedance of the resonator and each junction has a tunneling resistance  $R_T$ <sup>19</sup>. Consequently, we can tune the coupling strength  $\gamma_T$  by two orders of magnitude with the bias voltage, which makes it possible to accurately measure the Lamb shift of the resonator. The measured values for the coupling strength are in good agreement with the theoretical model<sup>19</sup> (Methods).

Figures 2e–f show the shift of the resonator frequency as a function of the bias voltage for the two samples. The natural frequency of a harmonic oscillator experiences a classical damping shift  $\approx \gamma_T^2/(8\omega_r)$  (not shown for clarity in figures) which, in our experimental setup, is in the range of few kHz and cannot explain the data. Interestingly the effective temperature of the environment increases as a function of the bias voltage (see Supplementary Fig. 4). However, contrary to the anharmonic systems, the harmonic oscillator has no ac Stark shift by the environment, that is, the energy level shifts are independent of the temperature of the environment<sup>6</sup>. Thus, we conclude that the observed shift of the resonator frequency is the Lamb shift induced by the broadband electromagnetic environment formed by the photon-assisted electron tunneling. In the following we confirm our conclusion by comparing the experimental results with a theoretical model.

We model the environment as a continuum of modes<sup>6</sup> characterized by their coupling strength  $\gamma_T(\omega)$  to the resonator. An environmental mode exchanges energy with the system only at resonance, being the principal mechanism for dissipation. Yet all the environmental modes are coupled to the system leading to the renormalization of its energy levels<sup>1,2,6</sup>. For a broadband environment, the corresponding resonator Lamb shift  $\omega_L = \omega_r - \omega_r^0$  is given by<sup>6</sup>

$$\omega_L = -\text{PV} \int_0^\infty \frac{d\omega}{2\pi} \left( \frac{\gamma_T(\omega)}{\omega - \omega_r^0} + \frac{\gamma_T(\omega)}{\omega + \omega_r^0} \right), \quad (2)$$

where PV indicates the Cauchy principal value integration and  $\omega_r^0$  is the resonator frequency at  $V = 0$  (see Methods for details).

The Lamb shift includes two parts: one originating from the static coupling and corresponding to the limit  $\omega_r^0 \rightarrow 0$  in equation (2) and the other, purely dynamic part<sup>28</sup>. In atomic systems<sup>1–5,9</sup>, the static part corresponds to the

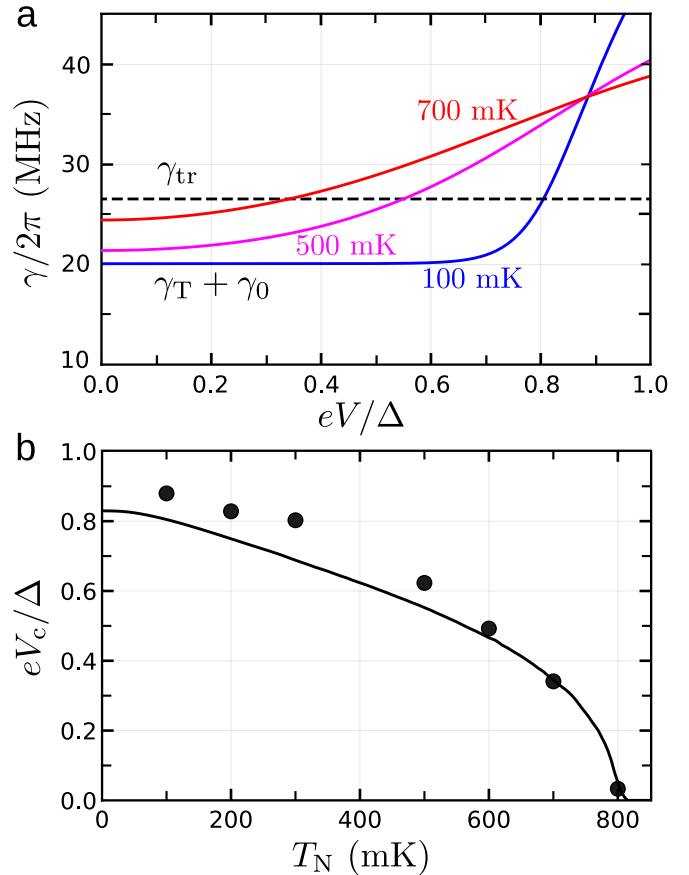


Figure 3. **Temperature dependence.** **a**, The calculated total coupling strength  $\gamma_T + \gamma_0$  as a function of the single-junction bias voltage at the normal-metal electron temperature  $T_N = 100$  mK (blue), 500 mK (magenta), and 700 mK (red) with parameters of Sample B (Table I). The horizontal dashed line indicates the coupling strength of the transmission line  $\gamma_{tr}$ . The coincidence point  $\gamma_T + \gamma_0 = \gamma_{tr}$  defines the critical bias value  $V_c$ , where the reflection coefficient ideally vanishes. The single-junction bias voltage is measured in the units of the  $T = 0$  superconductor gap  $\Delta/e$  and the theoretical calculation takes into account the temperature dependence of the gap. **b**, The critical voltage  $V_c$  as a function of the normal-metal electron temperature  $T_N$  for Sample B. The data points (filled circles) correspond to the bias voltage of the minima of the measured voltage reflection coefficients (Supplementary Fig. 5). For the calculated critical voltage (solid line) we use experimentally realized parameters (Table I) except that the value of the excess coupling strength is  $\gamma_0/2\pi = 20.1$  MHz capturing the enhanced losses by excess quasiparticles in the superconducting coplanar waveguide resonator at high temperatures.

additional electromagnetic mass owing to the environment which is already included in the measured masses of the particles. Thus the atomic spectra are sensitive only to the dynamic part and subtraction of the static part from the Lamb shift is necessary. This subtraction is identical to the celebrated Bethe renormalization<sup>2,29</sup>. Importantly, our experimental setup is sensitive to both of the contributions since we can access the resonator



when it is essentially decoupled from the environment. This is in stark contrast to the typical case of an atom where the electrons are always coupled to the electromagnetic environment. Note also that equation (2) is free of the rotating-wave approximation in the interaction between the resonator and the environment consisting of many modes. It is important not to make the rotating wave approximation since the shift arising from the co-rotating parts of the interaction [the first term in equation (2)] changes sign, and consequently, the shift arising from the counter-rotating parts of the interaction [the latter term in equation (2)] can make a non-negligible contribution to the total Lamb shift<sup>6,30</sup>. Here, indeed, approximately 57% of the total Lamb shift arises from the counter-rotating term at high bias voltages. As shown in Figs. 2e–f this theory yields an excellent agreement with the measured data.

To further verify the applicability of the theoretical model, we study the response of the coupling strength  $\gamma_T$  to the change in the normal-metal electron temperature  $T_N$ . We measure the critical bias point  $V_c$ , defined as the coincidence point  $\gamma_T + \gamma_0 = \gamma_{tr}$ , where the reflection ideally vanishes. In elevated normal-metal electron temperatures, the thermally activated electron tunneling is enhanced, which leads to an increased coupling strength  $\gamma_T$  in the subgap (Fig. 3a). As a result, the critical voltage moves to lower values (Fig. 3b). In elevated temperatures, the density of quasiparticles is increased in

the resonator, which leads to larger quasiparticle related losses<sup>31</sup>. To account for this, the excess coupling strength  $\gamma_0$  in Fig 3 is assumed larger than in the low temperature data of Table I. For simplicity, we assume it temperature independent. Overall, the good agreement between the measured and predicted critical voltages confirms that our model correctly captures the physics of the resonator environments.

In conclusion, we observed the Lamb shift induced by a broadband environment in an engineered quantum system. The Lamb shift was observed to be tunable in regimes where both the dynamical and static parts significantly contribute. We demonstrated that the environmental coupling strength is tunable over more than two orders of magnitude. To this end, we used bias-voltage-controlled electron tunneling in normal-metal–insulator–superconductor junctions, a device recently referred to as a quantum-circuit refrigerator<sup>14,15</sup>. Our results are in excellent agreement with first-principles theory<sup>19</sup>, which verifies the validity of the model not only for the Lamb shift but also for the quantum-circuit refrigerator<sup>14,15</sup>. Furthermore, our experiments expands the experimental operation regime of the quantum-circuit refrigerator to loaded quality factors up to  $10^3$  and internal quality factors above  $10^4$ , paving the way for rapid on-demand initialization of high-finesse quantum circuits, as well as the integration of the quantum-circuit refrigerator to synthetic quantum matter.

\* matti.silveri@oulu.fi

† mikko.mottonen@aalto.fi

- <sup>1</sup> W. E. Lamb and R. C. Retherford, Fine structure of the hydrogen atom by a microwave method, *Phys. Rev.* **72**, 241 (1947).
- <sup>2</sup> H. A. Bethe, The electromagnetic shift of energy levels, *Phys. Rev.* **72**, 339 (1947).
- <sup>3</sup> D. J. Heinzen and M. S. Feld, Vacuum radiative level shift and spontaneous-emission linewidth of an atom in an optical resonator, *Phys. Rev. Lett.* **59**, 2623 (1987).
- <sup>4</sup> M. Brune, P. Nussenzveig, F. Schmidt-Kaler, F. Bernardot, A. Maali, J. M. Raimond, and S. Haroche, From Lamb shift to light shifts: Vacuum and subphoton cavity fields measured by atomic phase sensitive detection, *Phys. Rev. Lett.* **72**, 3339 (1994).
- <sup>5</sup> M. Marrocco, M. Weidinger, R. T. Sang, and H. Walther, Quantum electrodynamic shifts of Rydberg energy levels between parallel metal plates, *Phys. Rev. Lett.* **81**, 5784 (1998).
- <sup>6</sup> H. J. Carmichael, *Statistical methods in quantum optics 1* (Springer, Berlin, Heidelberg, 1999).
- <sup>7</sup> N. Gisin and R. Thew, Quantum communication, *Nat. Photonics* **1**, 165 (2007).
- <sup>8</sup> T. D. Ladd, F. Jelezko, R. Laflamme, Y. Nakamura, C. Monroe, and J. L. O’Brien, Quantum computers, *Nature* **464**, 45 (2010).
- <sup>9</sup> T. Rentrop, A. Trautmann, F. Olivares, F. Jendrzejewski, A. Komnik, and M. Oberthaler, Observation of the phononic Lamb shift with a synthetic vacuum, *Phys. Rev.*

*X* **6**, 041041 (2016).

- <sup>10</sup> A. Fragner, M. Göppl, J. M. Fink, M. Baur, R. Bianchetti, P. J. Leek, A. Blais, and A. Wallraff, Resolving vacuum fluctuations in an electrical circuit by measuring the Lamb shift, *Science* **322**, 1357 (2008).
- <sup>11</sup> F. Yoshihara, T. Fuse, Z. Ao, S. Ashhab, K. Kakuyanagi, S. Saito, T. Aoki, K. Koshino, and K. Semba, Inversion of qubit energy levels in qubit-oscillator circuits in the deep-strong-coupling regime, *Phys. Rev. Lett.* **120**, 183601 (2018).
- <sup>12</sup> M. Mirhosseini, E. Kim, V. S. Ferreira, M. Kalaei, A. Sipahigil, A. J. Keller, and O. Painter, Superconducting metamaterials for waveguide quantum electrodynamics, [arXiv:1802.01708](https://arxiv.org/abs/1802.01708) (2018).
- <sup>13</sup> M. Partanen, K. Y. Tan, J. Govenius, R. E. Lake, M. K. Mäkelä, T. Tantt, and M. Möttönen, Quantum-limited heat conduction over macroscopic distances, *Nat. Phys.* **12**, 460 (2016).
- <sup>14</sup> K. Y. Tan, M. Partanen, R. E. Lake, J. Govenius, S. Masuda, and M. Möttönen, Quantum-circuit refrigerator, *Nat. Commun.* **8**, 15189 (2017).
- <sup>15</sup> S. Masuda, K. Y. Tan, M. Partanen, R. E. Lake, J. Govenius, M. Silveri, H. Grabert, and M. Möttönen, Observation of microwave absorption and emission from incoherent electron tunneling through a normal-metal-insulator-superconductor junction, *Sci. Rep.* **8**, 3966 (2018).
- <sup>16</sup> A. A. Houck, H. E. Türeci, and J. Koch, On-chip quantum simulation with superconducting circuits, *Nat. Phys.* **8**, 292 (2012).

- <sup>17</sup> M. Fitzpatrick, N. M. Sundaresan, A. C. Li, J. Koch, and A. A. Houck, Observation of a dissipative phase transition in a one-dimensional circuit QED lattice, *Phys. Rev. X* **7**, 011016 (2017).
- <sup>18</sup> R. Ma, B. Saxberg, C. Owens, N. Leung, Y. Lu, J. Simon, and D. I. Schuster, A dissipatively stabilized Mott insulator of photons, [arXiv:1807.11342](https://arxiv.org/abs/1807.11342) (2018).
- <sup>19</sup> M. Silveri, H. Grabert, S. Masuda, K. Y. Tan, and M. Möttönen, Theory of quantum-circuit refrigeration by photon-assisted electron tunneling, *Phys. Rev. B* **96**, 094524 (2017).
- <sup>20</sup> V. Gramich, P. Solinas, M. Möttönen, J. P. Pekola, and J. Ankerhold, Measurement scheme for the lamb shift in a superconducting circuit with broadband environment, *Phys. Rev. A* **84**, 052103 (2011).
- <sup>21</sup> G. S. Paraoanu, Microwave-induced coupling of superconducting qubits, *Phys. Rev. B* **74**, 140504 (2006).
- <sup>22</sup> C. Rigetti and M. Devoret, Fully microwave-tunable universal gates in superconducting qubits with linear couplings and fixed transition frequencies, *Phys. Rev. B* **81**, 134507 (2010).
- <sup>23</sup> J. Kerckhoff, H. I. Nurdin, D. S. Pavlichin, and H. Mabuchi, Designing quantum memories with embedded control: Photonic circuits for autonomous quantum error correction, *Phys. Rev. Lett.* **105**, 040502 (2010).
- <sup>24</sup> E. Kapit, J. T. Chalker, and S. H. Simon, Passive correction of quantum logical errors in a driven, dissipative system: A blueprint for an analog quantum code fabric, *Phys. Rev. A* **91**, 062324 (2015).
- <sup>25</sup> K. Geerlings, Z. Leghtas, I. M. Pop, S. Shankar, L. Frunzio, R. J. Schoelkopf, M. Mirrahimi, and M. H. Devoret, Demonstrating a driven reset protocol for a superconducting qubit, *Phys. Rev. Lett.* **110**, 120501 (2013).
- <sup>26</sup> G.-L. Ingold and Y. V. Nazarov, in *Single charge tunneling: Coulomb blockade phenomena in nanostructures*, edited by H. Grabert and M. H. Devoret (Plenum, New York, 1992).
- <sup>27</sup> R. C. Dynes, V. Narayanamurti, and J. P. Garno, Direct measurement of quasiparticle-lifetime broadening in a strong-coupled superconductor, *Phys. Rev. Lett.* **41**, 1509 (1978).
- <sup>28</sup> U. Weiss, *Quantum dissipative systems* (World Scientific, Berlin, Heidelberg, 2012).
- <sup>29</sup> A. Frisk Kockum, P. Delsing, and G. Johansson, Designing frequency-dependent relaxation rates and Lamb shifts for a giant artificial atom, *Phys. Rev. A* **90**, 013837 (2014).
- <sup>30</sup> G. S. Agarwal, Rotating-wave approximation and spontaneous emission, *Phys. Rev. A* **7**, 1195 (1973).
- <sup>31</sup> J. Goetz, F. Deppe, M. Haeberlein, F. Wulschner, C. W. Zollitsch, S. Meier, M. Fischer, P. Eder, E. Xie, K. G. Fedorov, E. P. Menzel, A. Marx, and R. Gross, Loss mechanisms in superconducting thin film microwave resonators, *J. App. Phys.* **119**, 015304 (2016).

**Acknowledgments** We acknowledge discussions with Jani Tuorila, Hermann Grabert, Aashish Clerk, Gianluigi Catelani, and Joonas Govenius. This research was financially supported by European Research Council under Grant No. 681311 (QUESS) and Marie Skłodowska-Curie Grant No. 795159; by Academy of Finland under its Centres of Excellence Program grants Nos. 312300, 312059 and grants Nos. 265675, 305237, 305306, 308161, 312300, 314302, 316551; JST ERATO Grant No. JPMJER1601, JSPS KAKENHI Grant No. 18K03486 and by the Alfred

Kordelin Foundation, the Emil Aaltonen Foundation, the Vilho, Yrjö and Kalle Väisälä Foundation, the Jane and Aatos Erkko Foundation, and the Technology Industries of Finland Centennial Foundation. We thank the provision of facilities and technical support by Aalto University at OtaNano – Micronova Nanofabrication Centre.

**Author contributions** M.S. carried out the theoretical analysis and wrote the manuscript with input from all the authors. S.M. and V.S. conducted the experiments and analyzed the data. S.M. and K.Y.T. fabricated the samples. R.E.L., M.P., and J.G. contributed to the fabrication, development of the devices and the measurement scheme. L.G. fabricated the niobium layers. E.H., M.P., and J.G. contributed in the data analysis. E.H. gave theory support. M.M. supervised the work in all respects.

**Competing interests** The authors declare no competing interests.

**Data availability** The data that support the findings of this study are available from the corresponding author upon reasonable request.

## METHODS

**Sample fabrication.** We fabricate the samples on 0.525-mm-thick silicon wafers. The silicon surface is passivated by a 300-nm-thick silicon oxide layer. We define the resonators by photolithography and ion etching of a 200-nm-thick sputtered niobium layer, and then cover them by a 50-nm-thick layer of  $\text{Al}_2\text{O}_3$ . We produce the superconductor–insulator–normal-metal junctions with electron beam lithography followed by two-angle evaporation. More fabrication details can be found in ref. 15.

**Measurements.** We use a commercial dilution refrigerator to cool the samples down to the base temperature of 10 mK. We attach the samples using vacuum grease to a sample holder with a printed circuit board, and bond them with aluminium wires. The printed circuit board is connected to the room-temperature setup by coaxial cables. The measurements are repeated multiple times.

The bias voltage is applied to the superconductor–insulator–normal-metal junctions by a battery-powered source. We measure the current through the junctions by a battery-powered transimpedance amplifier, which is connected to a voltmeter through an isolation amplifier. We measure the reflection coefficient of the sample with a vector network analyser. Based on the power level of the vector network analyser and total attenuation, the power of the signal reaching the sample is around  $-100$  dBm (Supplementary Fig. 2).

The quasiparticle temperature of the superconducting leads and the electron temperature of the normal-metal island differ from the base temperature due to leakage through the radiation shields. They also depend on the level of the probe signal. However, no significant changes were noticed in the range of powers from  $-95$  dBm to

−105 dBm.

**Photon-assisted electron tunneling.** Reference 19 details the theory of the photon-assisted tunneling at a normal-metal–insulator–superconductor junction. According to the theory, the photon-assisted tunneling forms an electromagnetic environment for a quantum circuit, such as a high-quality superconducting resonator. See also ref. 26 for a general overview on tunneling at nanostructures. For completeness, we present here the main results of the theory.

We consider a normal-metal–insulator–superconductor junction at the energy bias  $E$  and define the rate

$$\vec{F}(E) = \frac{1}{h} \int d\varepsilon n_S(\varepsilon)[1 - f_S(\varepsilon)]f_N(\varepsilon - E), \quad (3)$$

where  $\varepsilon$  denotes electron energy. The function  $\vec{F}(E)$  gives the normalized rate of forward quasiparticle tunneling for a junction with tunneling resistance  $R_T$  equal to the von Klitzing constant  $R_K = h/e^2$ . The tunneling rate is dictated by the occupations of the normal-metal and superconductors through the Fermi functions,  $f_N(\varepsilon)$  and  $f_S(\varepsilon)$ , respectively, as well as by the normalized quasiparticle density of the states in the superconductor

$$n_S(\varepsilon) = \left| \text{Re} \left\{ \frac{\varepsilon + i\gamma_D \Delta}{\sqrt{(\varepsilon + i\gamma_D \Delta)^2 - \Delta^2}} \right\} \right|, \quad (4)$$

where  $\Delta$  is the superconductor gap parameter and  $\gamma_D$  is the Dynes parameter (Table I). A photon-assisted tunneling event shifts the charge of the resonator by an amount of  $\Delta q = \alpha e$ , where  $\alpha = C_c/(C_c + C_{\Sigma m})$  is a capacitance fraction of the normal-metal island. The charge shift induces transitions from the resonator energy eigenstate  $|m\rangle$  to the eigenstate  $|m'\rangle$  ( $\ell = m' - m \geq 0$ ) through the matrix element

$$\begin{aligned} |M_{mm'}|^2 &= \left| \int \psi_{m'}^*(q - \alpha e) \psi_m(q) dq \right|^2 \\ &= e^{-\rho} \rho^\ell \frac{m!}{m!} [L_{m'}^\ell(\rho)]^2 \end{aligned} \quad (5)$$

where  $\psi_m(q) = \langle q|m\rangle$  are the resonator energy eigenstates represented in the  $q$  basis,  $\rho = \pi\alpha^2 Z_r/R_K$  is an interaction parameter expressed in terms of the characteristic impedance  $Z_r$  of the resonator, and  $L_{m'}^\ell(\rho)$  denote the generalized Laguerre polynomials.

The resonator transition rate becomes

$$\Gamma_{m,m'}(V) = |M_{mm'}|^2 \frac{2R_K}{R_T} \sum_{\tau=\pm 1} \vec{F}(\tau eV + \hbar\omega_r \ell - E_N), \quad (6)$$

where we have assumed that two superconductor–insulator–normal-metal junctions of the construction are sufficiently identical, the electrodes are at the same temperature, and that the charging energy  $E_N = e^2/2(C_c + C_{\Sigma m}) \sim h \times 10$  MHz of the normal-metal island is the smallest of the relevant energy scales of the setup ( $\Delta$ ,  $\hbar\omega_r$ , and  $k_B T_N$ ). In a typical experimental scenario, the interaction parameter  $\rho$  is far below unity since  $Z_r \ll R_K$ . Thus, at low powers the dominant transitions are those between adjacent states  $\Gamma_{m,m-1}$  and  $\Gamma_{m,m+1}$ . In this case, we characterize the electromagnetic environment through its coupling strength  $\gamma_T$  and effective temperature  $T_T$ ,

$$\gamma_T = \frac{2\pi C_c^2}{(C_c + C_{\Sigma m})^2} \frac{Z_r}{R_T} \sum_{\ell,\tau=\pm 1} \ell \vec{F}(\tau eV + \ell \hbar\omega_r - E_N), \quad (7a)$$

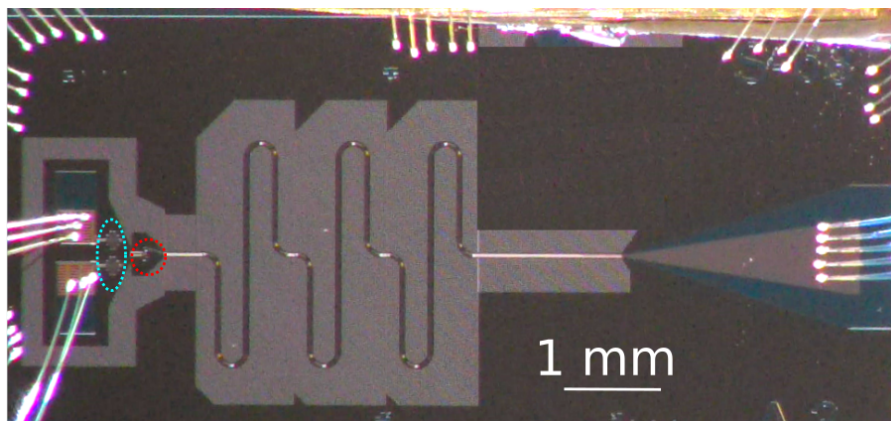
$$T_T = \frac{\hbar\omega_r}{k_B} \left[ \ln \left( \frac{\sum_{\tau=\pm 1} \vec{F}(\tau eV + \hbar\omega_r - E_N)}{\sum_{\tau=\pm 1} \vec{F}(\tau eV - \hbar\omega_r - E_N)} \right) \right]^{-1}, \quad (7b)$$

which are defined through the mapping  $\Gamma_{m,m-1} = \gamma_T(N_T + 1)m$  and  $\Gamma_{m,m+1} = \gamma_T N_T(m + 1)$  of the transition rates, where the mean number of excitations  $N_T = 1/[e^{\hbar\omega_r/(k_B T_T)} - 1]$  defines the effective mode temperature  $T_T$ . Here,  $k_B$  is the Boltzmann constant. Note that the quasiparticle tunneling, that is, the function  $\vec{F}(E)$  in equation (3), defines the dependence of the coupling strength and the temperature on the bias voltage  $V$  and the resonator frequency  $\omega_r$ .

**High-frequency behaviour.** As a  $1/\omega$  integral, the Lamb shift in equation (2) heavily depends on the high-frequency behaviour of the coupling strength  $\gamma_T(\omega)$  of equation (7a). Apart from the thermal activation regime occurring at biasing conditions near the gap edge, the electron tunneling forms an ohmic electromagnetic environment  $\gamma_T \propto \omega$ , see ref. 19. To calculate the theoretical curves in Fig. 2 we use experimental parameters of Table I, as well as the frequency and biasing dependence of the coupling strength  $\gamma_T$  of equation (7a). To make the integral of equation (2) convergent for an asymptotically ohmic environment, we add to the coupling strength the standard Drude cut-off  $\gamma_T(\omega)/(1 + \omega^2/\omega_c^2)^{28}$ , where the cut-off frequency  $\omega_c$  is extracted by fitting the theory to the data in Fig. 2e,f. We attribute the cut-off frequency partly to the higher modes of the coplanar waveguide resonator.

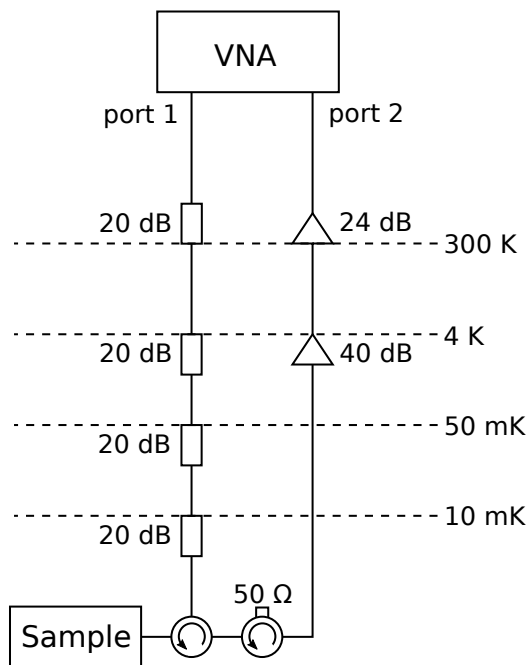
## Supplementary information: Observation of a broadband Lamb shift in an engineered quantum system

Matti Silveri, Shumpei Masuda, Vasilii Sevriuk, Kuan Y. Tan, Eric Hyppä,  
Matti Partanen, Jan Goetz, Russell E. Lake, Leif Grönberg, and Mikko Möttönen  
(Dated: December 16, 2022)

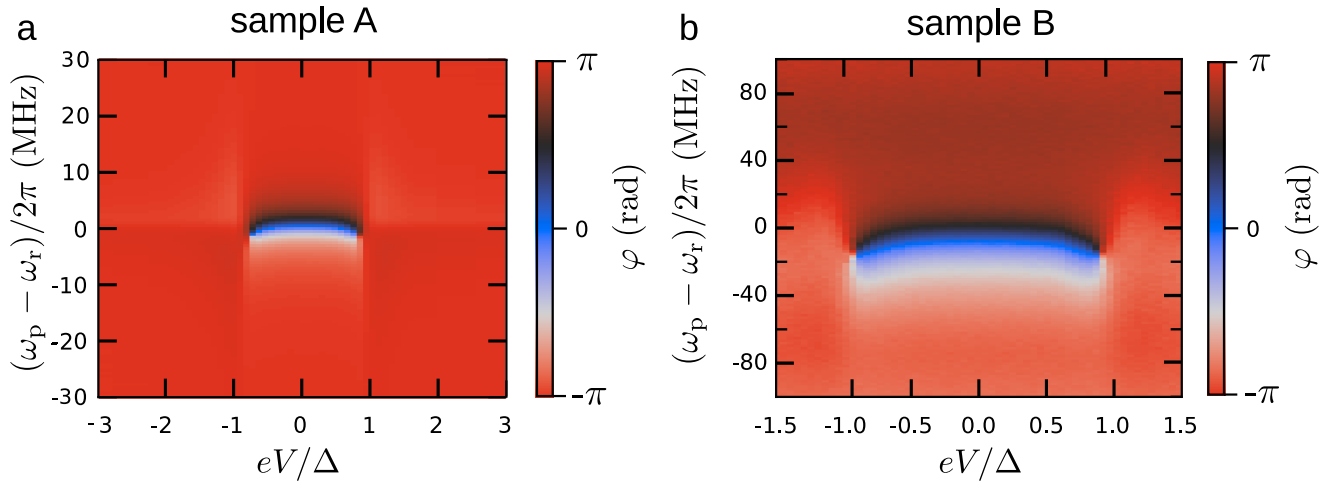


**Supplementary Figure 1 | Sample A.** Image of the device showing from left to right the  $RC$  filters (blue circle), the quantum-circuit refrigerator (red circle) comprising two superconductor–insulator–normal-metal tunnel junctions, the coplanar-waveguide resonator (meandering line), and the transmission line (straight horizontal line with tapering at the right end). Sample B is similar to Sample A except that it lacks the  $RC$  filters and its quantum-circuit refrigerator features two additional tunnel junctions employed as a thermometer for the normal-metal electron temperature<sup>14,15</sup>.

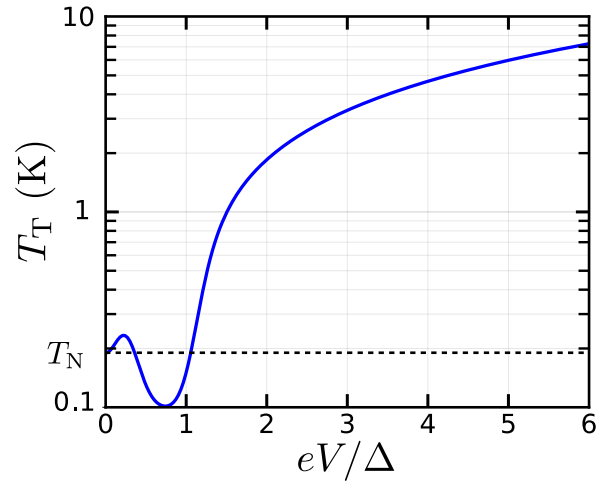




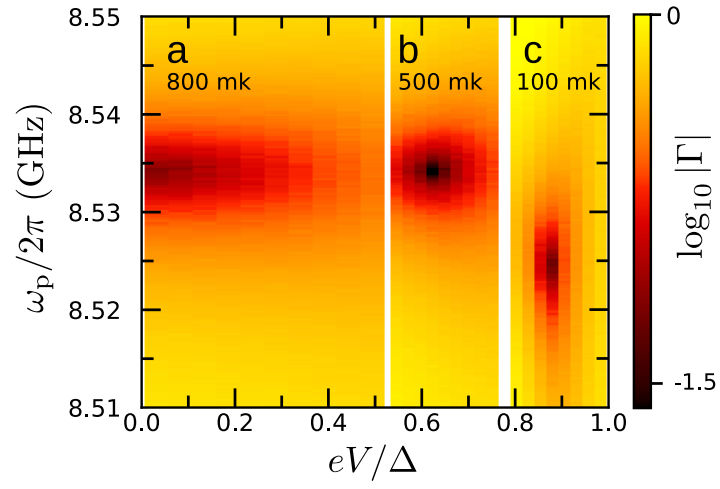
**Supplementary Figure 2 | Measurement setup for Sample B.** The signal going from port 1 of the vector network analyzer (VNA) to the sample is attenuated at different temperature stages as indicated, and the signal going from the sample to port 2 of the VNA is amplified at 4 K and at room temperature. A circulator is used to guide the input signal to the sample and the reflected signal via the amplifiers back to the VNA. Another circulator with a 50- $\Omega$  termination isolates the sample from the noise coming from the amplifier. The setup for Sample A is similar.



**Supplementary Figure 3 | Voltage reflection coefficient.** **a, b**, Phase of the voltage reflection coefficient  $\Gamma = |\Gamma| \exp(-i\varphi)$  as a function of the probe frequency  $\omega_p$  and the single-junction bias voltage  $V$  for Sample A and B.



**Supplementary Figure 4 | Electromagnetic environment.** Calculated temperature  $T_T$  of the environment as a function of the single-junction bias voltage  $V$  for Sample A with the parameters of Table I. At zero bias, the environment temperature equals the electron temperature  $T_N$  (dashed line) and at high bias it increases linearly.



**Supplementary Figure 5 | Temperature dependence.** **a–c**, Magnitude of the voltage reflection coefficient  $\Gamma = |\Gamma| \exp(-i\varphi)$  as a function of the probe frequency  $\omega_p$  and the single-junction bias voltage  $V$  for Sample B at the normal-metal electron temperature  $T_N = 800$  mK in **a**, 500 mK in **b**, and 100 mK in **c**.